Article

Understanding the Nature of Capacity Decay and Interface Properties in Li//LiNi$_{0.5}$Mn$_{1.5}$O$_4$ Cells by Cycling Aging and Titration Techniques

Sara Ahmad J. A. Al-Hail, Md Ruhul Amin,* Ramesh Kumar Petla, Umair Nisar, Rachid Essehli, Said Ahzi, and Ilias Belharouak*
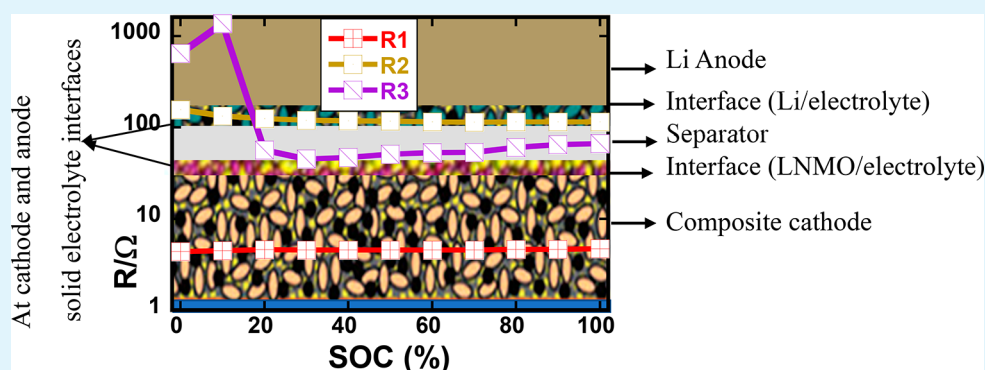
Read Online

ACCESS | Metrics & More | Article Recommendations | Supporting Information

ABSTRACT: The spinel structure LiNi$_{0.5}$Mn$_{1.5}$O$_4$ (LNMO) is a propitious cathode material for next-generation lithium-ion batteries for fast charge−discharge applications, but its capacity decay mechanism and rate-limiting process are not yet well understood. In this study, electrochemical impedance spectroscopy (EIS) with galvanostatic intermittent titration (GITT) and cycling aging techniques were employed to investigate the nature of capacity decay in disordered-phase LNMO. Different resistive components were separated after every 10 cycles. Cell overvoltages (ΔVs) due to ohmic conduction, charge transfer (CT), and concentration polarization (CP) were individually determined. Results revealed that the cell exhibited a higher ΔV at a higher discharged state. However, the ΔV value for CP was higher at a higher state of charge (SOC), and the overall LNMO/electrolyte interface played a major role in the rate-determining step. Battery life was estimated based on the results. Battery calendar life was found to be more vulnerable than cycle life. Results also indicated that the working SOC range could be optimized based on the resistance analysis by avoiding those SOCs that have the most detrimental impact (e.g., heat generation and fire hazard).

KEYWORDS: LiNi$_{0.5}$Mn$_{1.5}$O$_4$ spinel, lithium-ion batteries, cycling aging, capacity degradation, interfacial resistance, ionic diffusivity, GITT

1. INTRODUCTION

Since its commercial production in 1991,[1] the lithium-ion battery (LIB) has offered numerous energy storage options and has demonstrated high capability and versatility. It offers superior energy density, a minimum rate of self-discharge, and a long cycle life. Thus, it is used in a wide range of applications, including transportation electrification (e.g., hybrid, electric vehicles, and plug-in electric vehicles). In recent years, the success story of LIBs has garnered additional interest in the field of grid-scale energy storage. Apart from handling load fluctuations, this technology can provide a promising solution to challenges associated with grid-scale integration of renewable energy sources.[2,3]

The selection of a LIB cathode material is crucial as it determines the electrochemical performance of the battery, and it shares 40% of its total cost.[4] The gold standards of cathode materials used in current battery systems are LiMn$_2$O$_4$, LiCoO$_2$, LiNi$_{1/3}$Mn$_{1/3}$Co$_{1/3}$O$_2$, LiNi$_{0.5}$Mn$_{1.5}$O$_4$, LiFePO$_4$, LiNi$_{0.8}$Co$_{0.15}$Al$_{0.05}$O$_2$, and LiNi$_{0.5}$Co$_{0.2}$Mn$_{0.3}$O$_2$. However, almost all these materials have already reached the limit of their practical energy density. Among the different cathode materials, a spinel structure is particularly attractive due to its high operating voltage versus that of Li/Li$^+$ ($\sim$5 V). Specifically, LiNi$_{0.5}$Mn$_{1.5}$O$_4$ (LNMO) operates at a flat

potential plateau at 4.7 V, and its theoretical capacity is 147 mAh g^{-1}, which is close to other mass-produced materials including LiCoO$_2$ and LiFePO$_4$.[5−7] LNMO can be composed of two different space groups. The ordered group is a simple cubic phase $P4_332$ calcinated at temperatures less than 700 °C, where Ni, Mn, and Li occupy the 4a, 12d, and 4c sites, respectively. Conversely, the disordered space group is a $Fd\overline{3}m$ face-centered spinel, where Ni and Mn are randomly distributed on the 16d octahedral sites. Thermal treatment of LNMO at temperatures above 700 °C results in oxygen deficiency (LiNi$_{0.5}$Mn$_{1.5}$O$_{4-\mu}$) or nickel deficiency (Li-Ni$_{0.5-x}$Mn$_{1.5+x}$O$_{4-\delta}$), and both situations induce the partial reduction of Mn^{4+} to Mn^{3+} to compensate for charge balance due to nickel or oxygen deficiencies.[8−12]

Despite considerable research conducted in recent years, market penetration of LNMO has not been achieved for several key reasons due to a lack of understanding of the various governing performance factors. In the LNMO system, in addition to major cell-level challenges such as choice of electrolyte and anode and optimization of cell design, there still exists material-level impediments to commercialization, such as the rating-limiting factor, origin of overvoltage (ΔV), different resistive components, and battery performance decay, which govern the final calendar and cycle life of the envisioned Li-ion cells.

To mitigate the problem of performance degradation in a high-voltage spinel, several approaches could be adopted. First, Mn/Ni could be partially replaced with other metal ions, such as Cr^{3+}, Fe^{3+}, and Al^{3+}, to reduce the problem of Mn dissolution via enrichment of dopants and a deficiency of Ni. Second, Ni is responsible for electrolyte decomposition, causing a thick solid electrolyte interface (SEI) to form due to its high redox potential. For this reason, surface modification by coating reduces the interfacial interactions of the cathode with the adjacent electrolyte by suppressing the corrosion reaction serving as an HF scavenger.[13] Surface modification is achieved by using oxide coatings, including Al$_2$O$_3$, SiO$_2$, ZrO$_2$, TiO$_2$, MgO, and ZnO.[14,15] However, it is not known whether battery performance is limited by an interfacial charge transfer (CT) process due to continuous electrolyte decomposition or calendar life is more vulnerable than cycle life. Which resistive processes/components—ohmic, interfacial activation, or concentration polarization (CP)—significantly contribute to the cell ΔV under battery operating conditions is also not known. Apart from the cost of the coating process, a mechanistic understanding of uncoated LNMO is needed before surface engineering of the material.

For a given set of conditions, battery performance is evaluated by the capacity and power it can provide. As a matter of fact, capacity fade or power fade acts as an indicator of a cell's lifetime for an application. Voltage and current measurements are employed to determine capacity and power in general, which are critical in determining battery performance. Nonetheless, the relationship between current and voltage in LIBs is multiplex and depends on various internal and external parameters, including aging level, temperature, current density, state of charge (SOC), the thickness of the cell, and its components. In this study, bare, disordered LNMO cathode materials were prepared by simple sol−gel synthesis to investigate mass transport properties along with interfacial kinetics upon cycling aging. EIS with GITT and cycling aging techniques were employed to determine the nature of capacity decay in disordered LNMO as a function of SOC. Different resistive components were separated after every 10 cycles. The results revealed that battery calendar life is more vulnerable than cycle life and that cell ΔV is greater in a higher state of discharge. However, CP contributes significantly to the ΔV value at a higher SOC. Overall, battery rate performance is determined by CT resistance at the LNMO/electrolyte interface. The formation of SEI from a residual product of oxidative electrolyte decomposition and its increasing thickness resulted in a continual loss in capacity upon battery cycling. The battery life was estimated based on the results. Our articulation is that the CT resistance at the higher state of discharge is detrimental to the safety and performance of LNMO and can pose a fire hazard.

2. EXPERIMENTAL SECTION

2.1. Synthesis of LNMO Cathode Materials. Pure LNMO was prepared via a sol−gel synthesis process using lithium (99.0%), manganese (99.99%), and nickel (99.998%) acetates. All the chemicals were purchased from Sigma-Aldrich. Details of the synthesis procedure can be found elsewhere.[16] In brief, first of all the precursors in stoichiometric amounts were dissolved in 100 mL of distilled water. Then citric acid was added as a chelating agent in the precursor solution. The ammonia solution was used to adjust the pH of the solution to 8. The solution was continuous stirring at 80 °C until a gel was formed. The obtained gel was dried in a normal heating oven at 100 °C for 12 h and thereafter decomposed at 450 °C in the heating furnace for 6 h in air. Finally, the decomposed precursor was again calcined at 900 °C for 24 h at heating and cooling rates of 10 °C/min under an air atmosphere.

2.2. Characterization. The phase purities of the synthesized materials were identified by powdered X-ray diffraction (XRD) (Bruker D8 Advance) using Cu Kα radiation, with 2θ between 5° and 80° with a step size of 0.01°. The particle morphology (shape, size, and distribution) was investigated by field-emission scanning electron microscopy (Quanta FEG 650, FEI, USA). The symmetric and asymmetric vibrational bonds of the prepared disorder LNMO sample were recorded with KBr pellets by a Fourier-transform infrared spectroscopy (FTIR) spectrometer (Nicolet FT-NIR spectrometer, Thermo, USA).

2.3. Electrochemical Measurements. The cathodes were fabricated by making a slurry composed of active material (LNMO), conductive carbon black (Super-P), and poly(vinylidene fluoride) (PVDF) binder in a ratio of 75:17:8 in 1-methyl-2-pyrrolidone (NMP) as a solvent. A detailed discussion of electrode fabrication can be found elsewhere.[14] The slurry was thoroughly mixed for 6 h in a glass vial to form a homogeneous mixture. The slurry mixture was then cast on aluminum foil by using a doctor blade and dried in a vacuum oven at 100 °C to remove any traces of moisture and NMP. The electrodes were cut into circular disks 14.5 mm in diameter by using a puncher machine. The electrodes were ∼25 μm thick, and the material loading (active) was ∼10 mg cm^{-2} for each cell. The charge−discharge cycling measurements were performed by using CR2032 coin cells. An Ar-filled glovebox was used to assemble the cell, and lithium foil was used as the negative electrode. The liquid electrolyte composed of 1 M LiPF$_6$ was dissolved in a solvent of ethylene carbonate (EC) and dimethyl carbonate (DMC) (1:1 by v/v) mixture. The charge/discharge procedures were performed at room temperature in the constant current mode by using Solartron battery cyclers (1470E). The potential window was selected between 3.9 and 4.9 V for cycling the cells at different C-rates.

2.4. GITT and EIS Measurements. The GITT was used to partially delithiate/lithiate the cells. At the first cycle the cells were charged and discharged by using a current density equivalent to a rate of 0.1 C to form stable SEIs at both electrode interfaces (positive and negative electrode). While in the GITT measurement, the current (equivalent to 0.05 C) was applied to charge for 2 h to reach a certain SOC followed by a 3 h period at OCV to achieve a steady-state cell
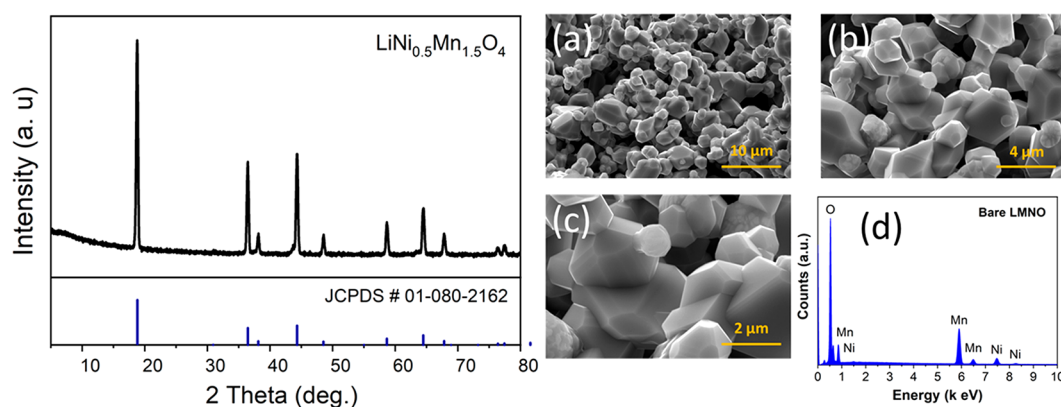
Figure 1. XRD patterns of the prepared LNMO along with JCPDS data and SEM images in different magnifications (a−c) and energy-dispersive X-ray spectroscopy spectra for the LNMO (d).

voltage. This experimental procedure was replicated stepwise for all states of charge and discharge. A detailed description of the experimental procedure can be found in our previous report.[14,23,29,32] While in galvanostatic titration, a difference of lithium concentration built up across the active particles. Consequently, lithium concentration polarization occurred when current was applied, followed by a relaxation of the cell voltage (depolarization) as the current was interrupted. After each partial lithium deintercalation/intercalation, the cells were allowed relaxing at OCV conditions to depolarize cell voltage and reach a steady state where voltage decay was <1 mV h^{-1} at the end of the time interval. At these situations, the cell voltage stands between the oxidation/reduction potential. Thereafter, EIS measurements were performed by using a Solartron battery cycler (1470E) in the frequency range of 1 MHz−50 mHz by using a sinusoidal voltage amplitude of 10 mV, which could induce partial delithiation/lithiation. The ionic diffusivity was then calculated by using the relaxation time as the derivative of the cell voltage during depolarization vs time. Details of the experimental procedure and data evaluation were discussed in a previous report.[17] The diffusion length is half of the average particle diameter. The measured EIS spectra were fitted with an equivalent circuit model built-in *Z-View* software.

2.5. Extensive Cycling Aging Test. The cell was ultimately charged and discharged for more than 700 cycles at a current rate of 1 C to examine the aging effect on LNMO and to investigate the interfacial impedance upon cycling. EIS measurements were performed after every 10 cycles. The analysis would help to understand how interfacial impedance, including CT resistance, varies upon cycling and whether ohmic resistance would remain unchanged or increase. Also, it could explain how cycling exacerbates the battery's life, catalyzed by components' deterioration. Thus, the study could quantify a battery's coulombic efficiency (CE) and predict cycle life. Cell impedance and voltage vs charge/discharge were plotted at the end of every 100 cycles for further assessments.

3. RESULTS AND DISCUSSION

3.1. Structural and Microstructural Characterization.

The XRD patterns for the as-synthesized LNMO are displayed in Figure 1. The material can be indexed to face-centered cubic space group $Fd\overline{3}m$ with $a = b = c = 8.17$ (JCPDS #80-2162), which agrees well with the formation of the spinel disordered phase (LiNi$_{0.5}$Mn$_{1.5}$O$_{4-\delta}$). All the observed Bragg peaks were strong and sharp, matching the reference peak position with (111) being the most intense.[9]

The SEM images of the as-prepared LNMO sample exhibit irregular particle morphology; however, most of the particles are octahedral in shape with an average particle size of 1.5 μm (Figure 1a−c). Furthermore, the electron dispersive X-ray spectroscopy (EDS) analysis (Figure 1d) revealed that the material was composed of Ni, Mn, and O, and there were no

element impurities. Thus, the LNMO material was well crystallized and free from any impurity phases.

The XRD measurements could not distinguish the disordered phase from the ordered phase since manganese and nickel exhibit similar X-ray light scattering patterns. FTIR was employed to reveal the characteristic vibrational bands of the ordered and disordered structure of the prepared LNMO sample (Figure S-1). The distinctive bands of the Mn/Ni−oxygen bonds between 700 and 400 cm^{-1} were used to evaluate the order of cations in the 16d sites of the spinel lattice. The very low intensity of the characteristics bands at 650, 556, 479, 467, and 430 cm^{-1} verified that the sample was disordered in the 16d octahedral sites.[6,18] The very strong band at 620 cm^{-1} was attributed to the Mn−O stretching mode, where two vibrations at 589 and 504 cm^{-1} were attributed to the Ni^{2+}−O stretching mode in the structure, and the results were in good agreement with previous reports.[5,19,20] The cyclic voltammetry (CV) at different scan rates (0.4−0.7 mV s^{-1}) and voltage ranges (3.5−4.9 V) are shown in Figure S-2. At 0.4 mV s^{-1}, three well-separated anodic peaks were observed at 4.1, 4.7, and 4.8 V, which represented Mn$^{3+/4+}$, Ni$^{2+/3+}$, and Ni$^{3+/4+}$ redox processes, respectively. Two-stage Li$^+$ deintercalation/intercalation from/into the electrode was confirmed by double peaks in the high-voltage range from 4.6 to 4.8 V. The appearance of the Mn redox peak at ∼4 V proved that the material was off-stoichiometric (disordered). As the scan rate increased, the anodic peaks shifted to higher potential values and the corresponding cathodic peaks to lower values, implying greater irreversibility associated with increasing CP. The LNMO sample in a half-cell configuration exhibited a voltage plateau of ∼4 V, which belonged to a Mn$^{3+/4+}$ redox couple.[21] Based on FTIR, cyclic voltammetry and charge−discharge results confirmed the formation of a disordered phase ($Fd\overline{3}m$).

3.2. GITT. GITT measurements were performed to separate the different resistive processes and determine ionic diffusivity as a function of SOC, the results of which would be used as a baseline for the aging effect. The GITT graph, as a function of time, is shown in Figure 2a. The cell was charged for 2 h to achieve 10% SOC followed by a 3 h relaxation time, where EIS was performed until full delithiation. Additionally, ionic diffusivity for the entire range of SOC was extracted from the depolarization cell voltage at OCV. The OCV (pseudoequilibrium) as a function of SOC was determined from the relaxation process of the GITT graph (cf. inset of Figure 2a). The cell initially exhibits low polarization followed
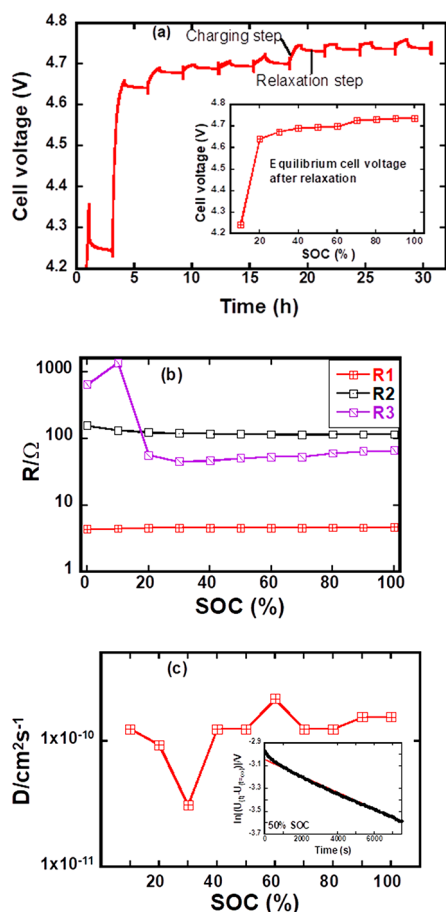
Figure 2. (a) GITT graph cell voltage vs time (inset is an equilibrium cell voltage extracted from relaxation process). (b) Extracted resistance of different processes as a function of the state of charge (SOC). (c) Lithium-ion diffusivity in $LiNi_{0.5}Mn_{1.5}O_4$ vs SOC (inset shows fitting the depolarization cell voltage as a function of time for 50% SOC).

by gradual increases during the charging at 4.6 V plateau. The electronic conductivity of LNMO decreased gradually as depletion of Mn^{3+} until all had turned to Mn^{4+}; the electronic conductivity was then at its lowest level, creating a low-voltage plateau. Once the Ni^{2+} ions started to oxidize, the conductivity significantly increased because of the creation of mixed-valence nickel (Ni^{2+}/Ni^{3+}). After that, the cell polarization reached around 4.75 V, when the removal of lithium continued over the second voltage plateau (Ni^{3+}/Ni^{4+}).[22] The Nyquist plots for every 10% SOC (from OCV to 100%) along with the fitted curve are presented in Figure S-3. The equivalent circuit model employed to fit the EIS data comprises seven-circuit elements, which is represented in Figure S-4. A detailed description of circuit elements can be found in our previous report.[14] Briefly, L_1 represents the induction of cell components and wires. R_1 is the high-frequency intercept due to ohmic transport losses in the electrolyte solution. R_2 is associated with the first semicircle CT resistance at the Li/electrolyte interface along with a resistance of electronic conductivity of active particle. R_3 is associated with the lower frequency second semicircle due to the CT reaction at LNMO/electrolyte interface (at the cathode side). Details about the equivalent circuit are given in the Supporting Information.

Different types of resistances separated from the impedance measurement are compared in Figure 2b as a function of SOC.

First, R_1 was constant throughout the experiment regardless of the state of delithiation because it was the cell uncompensated Ohmic resistance. Second, R_2 initially decreased and then became stable upon further delithiation, which was associated with an increase in the electronic conductivity once Ni became the active ion carriers due to the creation of a mixed-valence state, i.e., percolation network formation. Third, R_3 was high until 10% SOC, and then it stabilized, which explained the high acquired cell impedance. At the beginning R_3 started to increase due to the change of lower valence Mn^{3+} to Mn^{4+} in the course of the removal of Li ions at the 4 V plateau regime and outreached its maximum value at 10% SOC. The fast drop in R_3 corresponded to the enhanced electronic conductivity of LNMO due to the creation of the mixed-valence states of nickel (Ni^{2+}/Ni^{3+}), and then it kept almost constant with further removal of lithium.[23,24]

We extracted the ionic diffusivity as a function of SOC from the depolarization cell voltage of the GITT graph (Figure 2a). It should be noted that after each step of lithium removal the cell was relaxed under OCV conditions to attend the steady-state voltage. The relaxation (depolarization) cell voltage was fitted with the equation[25]

$$\ln\left(U_{(t)} - U_{(t=\infty)}\right) = \ln A - \frac{t}{\tau} \tag{1}$$

where A is the constant term for an invested material and $U_{(t)}$ and $U_{(t=\infty)}$ are the cell voltage at times t and $t = \infty$, respectively.

The slope of the plot $\ln\left(U_{(t)} - U_{(t=\infty)}\right)$ vs t provides the relaxation time, τ. The depolarization cell is nicely fitted with eq 1, as shown in the inset of Figure 2c. Details about the equation and its use and data evaluation are provided by Maier and Amin et al.[23,25] The ionic diffusivity of LNMO shows a gradual decrease and increase as a function of SOC (cf. Figure 2c), and the diffusivity values lie between 3×10^{-10} and 5×10^{-11} cm^2 s^{-1}, which are within the range of the reported values from 10^{-16} to 10^{-9} cm^2 s^{-1}.[14] Apparently, CT kinetics was rate-limiting; however, ionic diffusivity was relatively low and might be a rate-limiting factor at the higher current rate. Nonetheless, it was quite high to charge and discharge of a micrometer-size particles under practical current rates.[12]

3.3. Cycling Aging Studies. The cyclability and charged-discharged profile of LNMO vs Li half-cell are shown in Figure 3. The disordered LNMO shows 99% CE and 90% capacity retention after 700 cycles (Figure 3a). In the beginning, the cell capacity is very low but started to recover gradually and reached a maximum value of 102 mAh g^{-1}. Thereafter, the cell capacity started to fade slowly on cycling. The cell delivered discharge capacities of 82, 102, and 92 mAh g^{-1} at the 1st, 100th, and 700th cycles, respectively. The charge−discharge profile of first cycle is displayed in Figure S-5. Several factors might play a role in such a low initial discharge capacity, including oxidation of the electrolytes and intercalation of anions during the first-discharge cycle and prevention of electrolyte penetration on the whole surface of the active particle due to the partial agglomeration of active material and also due to cell fabrication process. Nonetheless, after 50 cycles, the cell showed stable electrochemical behavior for a prolonged period with gradual capacity fading. To gain further insight into the reason capacity fade happened in the LNMO electrode, EIS measurements were performed on the cycled cells in the discharged state. The EIS measurements were executed every 10th cycle to extract the different resistance
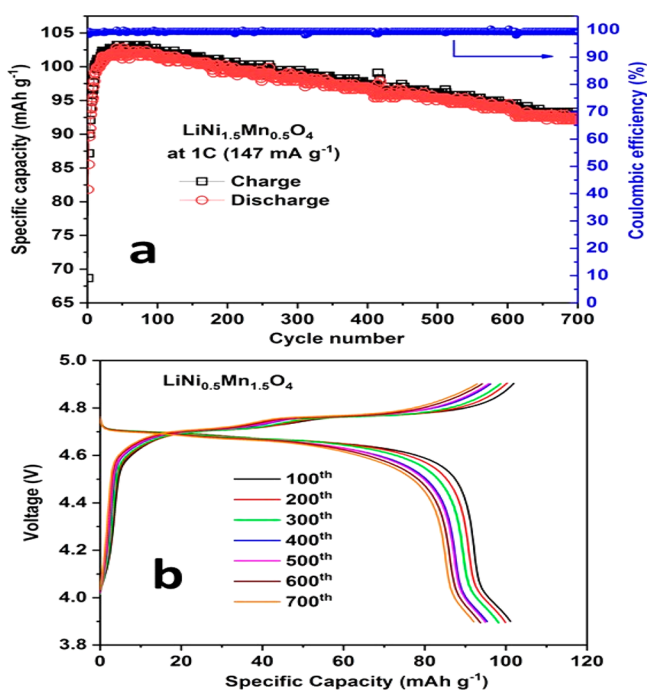
Figure 3. (a) Specific capacity as a function of cycling number (cyclability) and coulombic efficiency (b) and charge−discharge curves of $LiNi_{0.5}Mn_{1.5}O_4$ (LNMO) at 1 C rate for after every 100 cycles.

processes. It should be noted that after discharge the cell was relaxed for 2 h before EIS measurements were taken to keep the cell voltage in the steady-state condition. In such a situation, the cell voltage lies in between the oxidation−reduction potential, and a small applied amplitude would reduce the redox process during impedance measurements. The pattern of impedance spectra was similar to that given in Figure S3 obtained from GITT measurements. A detailed discussion of the equivalent circuit and data evaluation are given in the Supporting Information.

The three different resistances are plotted as a function of cycle number (cf. Figure 4). As shown in Figure 4, R_1 increased
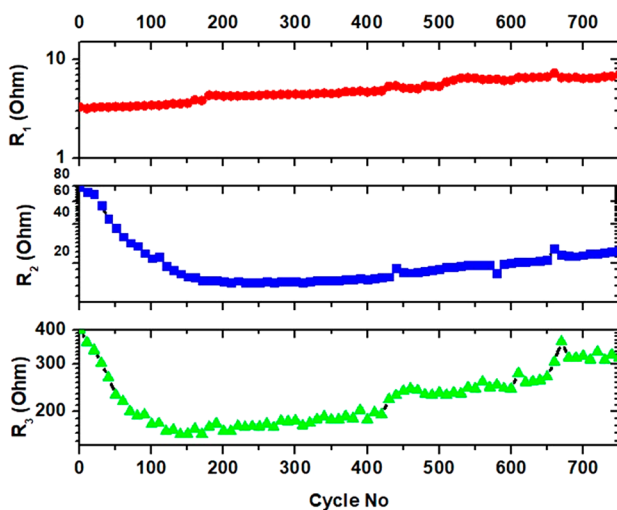

Figure 4. Comparison of individual cell resistances (ohmic and interfacial) extracted from EIS measurements of LNMO half-cell as a function of cycle number.

gradually due to the formation of the SEI both at the anode and cathode sides as it got thicker upon cycling associated with the reduction of Li concentration in the electrolyte solution; therefore, the ionic conductivity of electrolyte solution decreased. At the end of the 700th cycle, the R_1 value was almost double that of its initial value, which clearly indicated that electrolyte degradation took place gradually rather than the stable, protective SEI at the beginning of a couple of cycles. R_2 and R_3 decreased gradually upon charge−discharge up to 150 cycles. Thereafter, both started to increase slowly and gradually, which is consistent with the electrochemical performance of the cell, as shown in Figure 3. As mentioned above, R_2 is associated with the CT process at the Li/electrolyte interface along with the change in electronic conductivity of the active particles, whereas R_3 is associated with the CT process at the LNMO/electrolyte interface. Because of the formation of SEI and consumption of Li during the initial cycling, the electronic conductivity of the active particles gradually increased due to the formation of defects at the highly conductive region of the mixed-valence state; hence, R_2 could decrease. Although the cell was supposed to be entirely lithiated in the discharge state, some lithium might be uncompensated, and a single-valence state could not be achieved, which ultimately influenced the R_2 value. Then, R_2 increased as the thickness of SEI increased, which might block the active area, increasing the CT resistance part of R_2. In the beginning, R_3 was at its maximum value where the cathode surface area was not completely exposed to the electrolyte, which might later have come in contact upon cycling. Moving from the single- to mixed-valence state resulted in a drop in R_3, which then slowly increased with cycling because of increasing thickness of the SEI at the cathode side, along with the degradation process.[7,26] In the discharged state, the R_2 value was much less than the R_3 value, but they shared the same pattern. Also noticed was that as R_2 and R_3 decreased initially, the capacity of the battery increased as well (as will be explained). Thereafter, R_1, R_2, and R_3 increased, driving the capacity down at the same trend due to cell degradation and consumption of Li forming SEI. Generally, the increase in R_1, R_2, and R_3 resulted in increasing impedance of EIS measurement; nevertheless, the limiting factor was the CT resistance at the cathode−electrolyte interface, i.e., R_3.

Figure 3a indicates that the cell capacity gradually improved up to 55 cycles because the particles became more active upon cycling, as the surfaces of the particles were partially exposed during the initial cycling. The highest capacity reached was 102 mAh g^{-1}, while the lowest was 92 mAh g^{-1} at the end of the experiment. The system was stable, with a percentage decrease of 1.4% after every 100 cycles, excluding the first 100 cycle, where the resistance was very high. The battery would reach 90% of its original capacity after 700 cycles, matching the experimental results, and was expected to reach 50% of its initial capacity after 3500 cycles. Based on this calculation, a battery could be selected for a particular application, and the cycle life could be estimated as well.[25,26,28] The coulombic efficiency of electrode materials is an essential factor for excellent cycling performance of the battery. The cell exhibited a slight increase in CE after the first 100 cycles and then gradually dropped for the next 600 cycles. Moreover, it showed a capacity retention of 90% for the entire cycling period from 102 to 92 mAh g^{-1} for 700 cycles. The purpose of this work is to study the aging effect on a high-voltage spinel; hence, a relatively high cycle rate was applied. The loss of active

material and the accumulation of CT impedance were attributed to poor initial CE.

At a given set of conditions, the voltage and current measurements were employed to determine capacity and power in general, which are critical factors in determining the battery performance.[25,26,29] However, the relationship between current and voltage in LIBs is multiplex and depends on various internal and external parameters such as current density, SOC, the aging level, temperature, and the geometry of the cell and its components.[30]

In a battery cell, the accessible electrical energy can be derived from the change in Gibbs free energy of the redox reaction used in the cell.[31]

$$\Delta G = -\eta \cdot F \cdot OCV \qquad (2)$$

where OCV stands for open circuit voltage, η is the exchanged number of electrons in the reaction, and F is the Faraday constant (96487 C mol^{-1}). It should be noted that all the accessible cell energy (at equilibrium) cannot be converted into useful electrical energy due to loss of some extent while current flows through the cell and its potential (cell voltage) departs from the OCV and lessening the amount of energy that can be converted into a useful one. As an example, the equilibrium cell voltage is compared with the cell charged after every 100th cycles at 1 C as a function of SOC in Figure 5. The
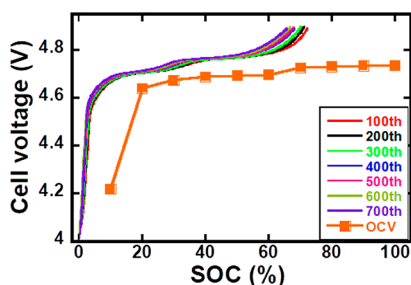

Figure 5. Comparison between open circuit voltage (extracted from relaxation process) and cell charged after every 100th cycles at 1 C as a function of the state of charge (SOC).

ΔV resulted from the cell's either charge or discharge process is originated by electronic and ionic conduction, ionic diffusion, and CT processes.[32] The higher magnitude of the ΔV causes the charge/discharge cutoff voltage to be reached earlier than expected. In addition, if the ΔV increases, more energy will be lost as heat and thus will limit the capacity and the power capabilities of the cells. Normally, contributions to the ΔV can be divided into two parts: ohmic and non-ohmic impacts. Noted that the ohmic effect is a solely resistive process and exhibits a linear relationship between current and voltage at under applied load.[32] The ohmic resistance is caused by the contributions of the electronic resistances of the active materials, the ionic resistance of the electrolyte solution, the interfaces between electrodes and current collectors, and the electrical tabs.[33] The non-ohmic segment of ΔV is related to CPs and polarization losses and comprises activation. It should be mentioned that the activation polarization propels the redox reaction at the electrode/electrolyte interface, and it is related to a CT process.[33,34]

In general, the total ΔV associated in a cell under operational conditions can be denoted as the CT at both electrode surfaces, ionic diffusion, and the ohmic conduction:[32]

$$n = R_1(\text{electrolyte}) + R_2\left(\frac{\text{Li}}{\text{electrolyte}} + \text{active particle}\right)$$
$$+ R_3\left(\frac{\text{LNMO}}{\text{electrolyte}}\right) + R_D(\text{ionic diffusion}) \qquad (3)$$

In the linear functioning zone of the cells, in terms of current (I)−resistance (R), the ΔV can be written as[32]

$$\Delta V = R \cdot I \qquad (4)$$

Thus, to obtain the various contributions to ΔV, we used the results of the impedance analysis from the Figure 4 after every 100 cycles in the fully discharged state considering a current rate of 1 C. The results are compared in Figure 6a as a function
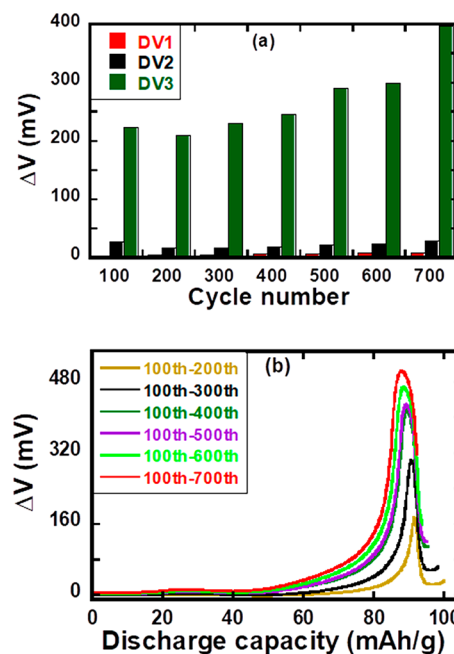

Figure 6. (a) Individual contribution of different resistive processes (obtained from discharge state) on the overpotential derived from a current rate of 1 C and (b) relative cell overpotential after every 100th cycle as a function of discharge capacity. Here ΔV_1, ΔV_2, and ΔV_3 correspond to the obtained R_1, R_2, and R_3.

of cycle number, and the majority of cell voltage polarization was found to be associated with CT process at LNMO/electrolyte interface. In addition, the relative cell overpotential was calculated from the discharge voltage of Figure 3b after every 100 cycles and compared in Figure 6b as a function of capacity. It is discernible from Figure 6b that in the fully discharged state the cell exhibited the highest ΔV, which is consistent with the impedance measurements. Moreover, the overpotential due to the CP needed to be deconvoluted as a function of SOC. EIS measurements were performed every 10% SOC and deconvoluted the different resistances, as mentioned above. The individual resistances are compared in Figure 2b as a function of SOC. The ΔV was calculated and displayed in Figure 7a (for a current rate of 1 C) as a function of SOC, which included the CT and ohmic contributions.

It should be noted that the highest cell polarization was observed at around 10% SOC, which might be due to the conversion of all mixed-valence Mn$^{4+/3+}$ into a single-valence Mn^{4+}. Nonetheless, the total cell overpotential was derived
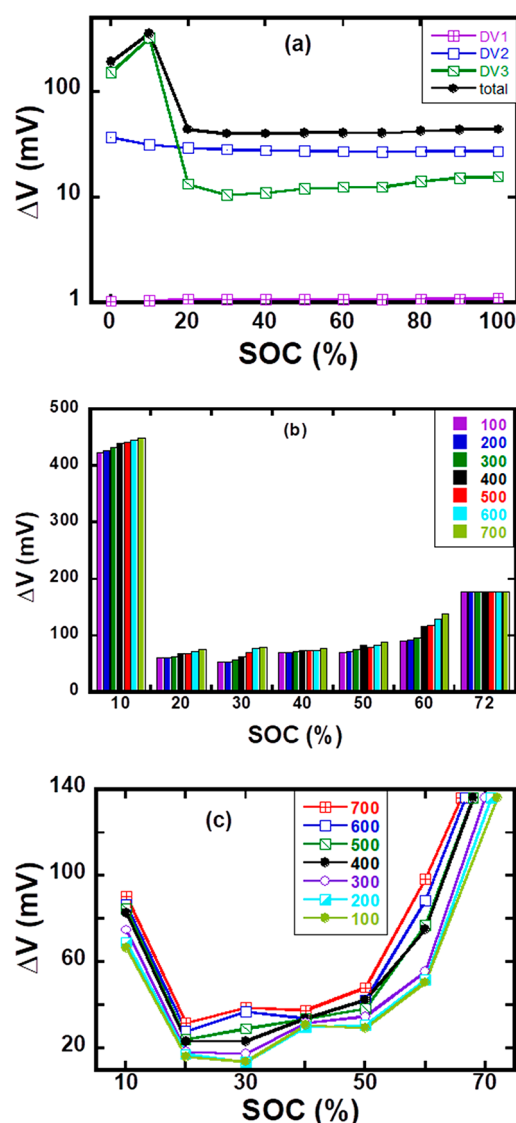
Figure 7. (a) Cell ΔV for individual resistances (obtained from impedance measurements after the relaxation of the cell) for a current rate of 1 C as a function of SOC. (b) Total cell polarization after every 100 cycles as a function of SOC. (c) ΔV due to the CP for every 100 cycles.

from the differences between the equilibrium cell voltage (given inset of Figure 2a) and cell voltage after every 100 cycles in Figure 5 as a function of SOC. The obtained data are displayed in Figure 7b. The cell ΔV gradually increased in every SOC calculated from cycle number 100 to 700. However, the enhancement of cell ΔV due to aging is not extremely significant.

The concentration ΔV was obtained from the differences of Figures 7a and 7b as a function of SOC and is displayed in Figure 7c. The overpotential due to CP exhibited complex behavior, gradually decreased, and at certain SOC again started to increase in a similar fashion. The ΔV value due to CP is higher at higher SOC. Because ionic diffusivity exhibited complex behavior, the CP would exhibit a similar ΔV profile.

4. CONCLUSION

In this work, we prepared disordered LNMO cathode material using a simple sol−gel method and characterized the material by XRD, FTIR, SEM, and cyclic voltammetry. The prepared disordered LNMO delivers a stable discharge capacity of 102 mAh g^{-1} at 1 C rate. The EIS with GITT and cycling aging techniques were employed to investigate the nature of capacity decay in disordered LNMO as a function of SOC. Different resistive components were separated after every 10 cycles. Battery calendar life was found to be more vulnerable than cycle life. The results showed that ΔV is higher in a higher state of discharge. However, CP contributed significantly to the value of ΔV at the higher SOC. Overall, battery rate performance is determined by CT resistance at the LNMO/ electrolyte interface. The formation of SEI from a residual product of oxidative electrolyte decomposition and its increasing thickness resulted in the continual loss of capacity upon battery cycling. Battery life was estimated based on the obtained results. Our articulation is that the CT resistance at the higher state of discharge is detrimental to the safety and performance of LNMO and poses a fire hazard.

■ ASSOCIATED CONTENT

ⓢ Supporting Information

The Supporting Information is available free of charge at https://pubs.acs.org/doi/10.1021/acsaem.0c00614.

Additional physical and electrochemical characterizations of the material, which include FTIR, CV at different scan rates, and Nyquist plots for EIS spectra for a half-cell at different SOC; the electrical equivalent circuit model (ECM) used for fitting the EIS data and extended expected long-term cycling (PDF)

■ AUTHOR INFORMATION

Corresponding Authors

Md Ruhul Amin − Energy and Transportation Science Division, Oak Ridge National Laboratory, Oak Ridge, Tennessee 37830, United States; ⓞ orcid.org/0000-0002-0054-3510; Email: aminr@ornl.gov

Ilias Belharouak − Energy and Transportation Science Division, Oak Ridge National Laboratory, Oak Ridge, Tennessee 37830, United States; Bredesen Center for Interdisciplinary Research and Graduate Education, Knoxville, Tennessee 37996, United States; ⓞ orcid.org/0000-0002-3985-0278; Email: belharouaki@ornl.gov

Authors

Sara Ahmad J. A. Al-Hail − Energy and Transportation Science Division, Oak Ridge National Laboratory, Oak Ridge, Tennessee 37830, United States; Qatar Environment and Energy Research Institute, Hamad Bin Khalifa University, Qatar Foundation, 34110 Doha, Qatar

Ramesh Kumar Petla − Qatar Environment and Energy Research Institute, Hamad Bin Khalifa University, Qatar Foundation, 34110 Doha, Qatar; ⓞ orcid.org/0000-0001-9456-3370

Umair Nisar − Center for Advanced Materials (CAM), Qatar University, 2713 Doha, Qatar; ⓞ orcid.org/0000-0002-3690-8286

Rachid Essehli − Energy and Transportation Science Division, Oak Ridge National Laboratory, Oak Ridge, Tennessee 37830, United States

Said Ahzi − Qatar Environment and Energy Research Institute, Hamad Bin Khalifa University, Qatar Foundation, 34110 Doha, Qatar

Complete contact information is available at:
https://pubs.acs.org/10.1021/acsaem.0c00614

Notes

The authors declare no competing financial interest.

■ REFERENCES

(1) Nitta, N.; Wu, F.; Lee, J. T.; Yushin, G. Li-Ion Battery Materials: Present and Future. *Mater. Today* **2015**, *18* (5), 252−264.

(2) Kousksou, T.; Bruel, P.; Jamil, A.; El Rhafiki, T.; Zeraouli, Y. Energy Storage: Applications and Challenges. *Sol. Energy Mater. Sol. Cells* **2014**, *120*, 59−80.

(3) Hu, M.; Pang, X.; Zhou, Z. Review Recent Progress in High-Voltage Lithium Ion Batteries. *J. Power Sources* **2013**, *237*, 229−242.

(4) Wakihara, M. Recent Developments in Lithium Ion Batteries. *Mater. Sci. Eng., R* **2001**, *33* (4), 109−134.

(5) Kunduraci, M.; Amatucci, G. G. Synthesis and Characterization of Nanostructured 4.7 V Li[Sub x]Mn[Sub 1.5]Ni[Sub 0.5]O[Sub 4] Spinels for High-Power Lithium-Ion Batteries. *J. Electrochem. Soc.* **2006**, *153* (7), A1345.

(6) Kunduraci, M.; Al-Sharab, J. F.; Amatucci, G. G. High-Power Nanostructured LiMn 2-XNi XO 4 High-Voltage Lithium-Ion Battery Electrode Materials: Electrochemical Impact of Electronic Conductivity and Morphology. *Chem. Mater.* **2006**, *18* (15), 3585−3592.

(7) Kovacheva, D.; Markovsky, B.; Salitra, G.; Talyosef, Y.; Gorova, M.; Levi, E.; Riboch, M.; Kim, H. J.; Aurbach, D. Electrochemical Behavior of Electrodes Comprising Micro- and Nano-Sized Particles of LiNi0.5Mn1.5O4: A Comparative Study. *Electrochim. Acta* **2005**, *50* (28), 5553−5560.

(8) Chen, Y.; Sun, Y.; Huang, X. Origin of the Ni/Mn Ordering in High-Voltage Spinel LiNi0.5Mn1.5O4: The Role of Oxygen Vacancies and Cation Doping. *Comput. Mater. Sci.* **2016**, *115*, 109−116.

(9) Xue, Y.; Wang, Z.; Zheng, L.; Yu, F.; Liu, B.; Zhang, Y.; Ke, K. Investigation on Preparation and Performance of Spinel LiNi0.5 Mn1.5 O4 with Different Microstructures for Lithium-Ion Batteries. *Sci. Rep.* **2015**, *5*, 1−11.

(10) Wu, Q.; Zhang, X.; Sun, S.; Wan, N.; Pan, D.; Bai, Y.; Zhu, H.; Hu, Y.-S.; Dai, S. Improved Electrochemical Performance of Spinel LiMn1.5Ni0.5O4 through MgF2 Nano-Coating. *Nanoscale* **2015**, *7* (38), 15609−15617.

(11) Lin, M.; Ben, L.; Sun, Y.; Wang, H.; Yang, Z.; Gu, L.; Yu, X.; Yang, X. Q.; Zhao, H.; Yu, R.; et al. Insight into the Atomic Structure of High-Voltage Spinel LiNi0.5Mn1.5O4 Cathode Material in the First Cycle. *Chem. Mater.* **2015**, *27* (1), 292−303.

(12) Xia, H.; Lu, L.; Lai, M. O. Li Diffusion in LiNi0.5Mn0.5O2 Thin Film Electrodes Prepared by Pulsed Laser Deposition. *Electrochim. Acta* **2009**, *54* (25), 5986−5991.

(13) Deng, J.; Xu, Y.; Xiong, L.; Li, L.; Sun, X.; Zhang, Y. Improving the Fast Discharge Performance of High-Voltage LiNi0.5Mn1.5O4 Spinel by Cu2+, Al3+, Ti4+ Tri-Doping. *J. Alloys Compd.* **2016**, *677*, 18−26.

(14) Nisar, U.; Amin, R.; Essehli, R.; Shakoor, R. A.; Kahraman, R.; Kim, D. K.; Khaleel, M. A.; Belharouak, I. Extreme Fast Charging Characteristics of Zirconia Modified LiNi0.5Mn1.5O4 Cathode for Lithium Ion Batteries. *J. Power Sources* **2018**, *396*, 774−781.

(15) Aoshima, T.; Okahara, K.; Kiyohara, C.; Shizuka, K. Mechanisms of Manganese Spinels Dissolution and Capacity Fade at High Temperature. *J. Power Sources* **2001**, *97−98*, 377−380.

(16) Nisar, U.; Al-Hail, S. A. J. A.; Petla, R. K.; Shakoor, R. A.; Essehli, R.; Kahraman, R.; AlQaradawi, S. Y.; Kim, D. K.; Belharouak, I.; Amin, M. R. Understanding the Origin of the Ultrahigh Rate Performance of a SiO2-Modified LiNi0.5Mn1.5O4 Cathode for Lithium-Ion Batteries. *ACS Appl. Energy Mater.* **2019**, *2* (10), 7263−7271.

(17) Amin, R.; Belharouak, I. Part II: Exchange current density and ionic diffusivity studies on ordered and disordered spinel LiNi$_{0.5}$Mn$_{1.5}$O$_4$ cathode. *J. Power Sources* **2017**, *348*, 318−325.

(18) Jin, Y.-C.; Lin, C.-Y.; Duh, J.-G. Improving Rate Capability of High Potential LiNi0.5Mn1.5O4-x Cathode Materials via Increasing Oxygen Non-Stoichiometries. *Electrochim. Acta* **2012**, *69*, 45−50.

(19) Kim, J. H.; Huq, A.; Chi, M.; Pieczonka, N. P. W.; Lee, E.; Bridges, C. A.; Tessema, M. M.; Manthiram, A.; Persson, K. A.; Powell, B. R. Integrated Nano-Domains of Disordered and Ordered Spinel Phases in LiNi0.5Mn1.5O4 for Li-Ion Batteries. *Chem. Mater.* **2014**, *26* (15), 4377−4386.

(20) Wang, J.; Lin, W.; Wu, B.; Zhao, J. Porous LiNi0.5Mn1.5O4 Sphere as 5 V Cathode Material for Lithium Ion Batteries. *J. Mater. Chem. A* **2014**, *2* (39), 16434−16442.

(21) Monaco, S.; De Giorgio, F.; Da Col, L.; Riché, M.; Arbizzani, C.; Mastragostino, M. Electrochemical Performance of LiNi0.5Mn1.5O4 Composite Electrodes Featuring Carbons and Reduced Graphene Oxide. *J. Power Sources* **2015**, *278*, 733−740.

(22) Moorhead-Rosenberg, Z.; Huq, A.; Goodenough, J. B.; Manthiram, A. Electronic and Electrochemical Properties of Li1-XMn1.5Ni0.5O4 Spinel Cathodes As a Function of Lithium Content and Cation Ordering. *Chem. Mater.* **2015**, *27* (20), 6934−6945.

(23) Amin, R.; Belharouk, I. Part I: Electronic and Ionic Transport Properties of the Ordered and Disordered LiNi0.5Mn1.5O4spinel Cathode. *J. Power Sources* **2017**, *348*, 311−317.

(24) Ma, J.; Hu, P.; Cui, G.; Chen, L. Surface and Interface Issues in Spinel LiNi0.5Mn1.5O4: Insights into a Potential Cathode Material for High Energy Density Lithium Ion Batteries. *Chem. Mater.* **2016**, *28* (11), 3578−3606.

(25) Maier, J. *Physical Chemistry of Ionic Materials: Ions and Electrons in Solids*; John Wiley & Sons: 2004.

(26) Nishikawa, K.; Zettsu, N.; Teshima, K.; Kanamura, K. Intrinsic Electrochemical Characteristics of One LiNi0.5Mn1.5O4 Spinel Particle. *J. Electroanal. Chem.* **2017**, *799* (June), 468−472.

(27) Li, J.-F.; Lin, C.-H.; Chen, K.-C. Cycle Life Prediction of Aged Lithium-Ion Batteries from the Fading Trajectory of a Four-Parameter Model. *J. Electrochem. Soc.* **2018**, *165* (16), A3634−A3641.

(28) Hendricks, C.; Williard, N.; Mathew, S.; Pecht, M. A Failure Modes, Mechanisms, and Effects Analysis (FMMEA) of Lithium-Ion Batteries. *J. Power Sources* **2015**, *297*, 113−120.

(29) Amin, R.; Chiang, Y. M. Characterization of Electronic and Ionic Transport in Li1-XNi0.33Mn0.33Co0.33O2 (NMC333) and Li1-XNi0.50Mn0.20Co0.30O2 (NMC523) as a Function of Li Content. *J. Electrochem. Soc.* **2016**, *163* (8), A1512−A1517.

(30) Berecibar, M.; Gandiaga, I.; Villarreal, I.; Omar, N.; Van Mierlo, J.; Van Den Bossche, P. Critical Review of State of Health Estimation Methods of Li-Ion Batteries for Real Applications. *Renewable Sustainable Energy Rev.* **2016**, *56*, 572−587.

(31) Murnane, M.; Ghazel, A. A Closer Look at State of Charge (SOC) and State of Health (SOH) Estimation Techniques for Batteries. *Analog Devices*, 2017.

(32) Amin, R.; Chiang, Y.-M. Characterization of Electronic and Ionic Transport in Li 1- x Ni 0.33 Mn 0.33 Co 0.33 O 2 (NMC 333) and Li 1- x Ni 0.50 Mn 0.20 Co 0.30 O 2 (NMC 523) as a Function of Li Content. *J. Electrochem. Soc.* **2016**, *163* (8), A1512−A1517.

(33) Ter Heijne, A.; Schaetzle, O.; Gimenez, S.; Fabregat-Santiago, F.; Bisquert, J.; Strik, D. P. B. T. B.; Barrière, F.; Buisman, C. J. N.; Hamelers, H. V. M. Identifying Charge and Mass Transfer Resistances of an Oxygen Reducing Biocathode. *Energy Environ. Sci.* **2011**, *4* (12), 5035−5043.

(34) Zhou, J.; Danilov, D.; Notten, P. H. L. A Novel Method for the in Situ Determination of Concentration Gradients in the Electrolyte of Li-Ion Batteries. *Chem. - Eur. J.* **2006**, *12* (27), 7125−7132.